4-28-2023

Volcano Opto-Acoustics: Mapping the Infrasound Wavefield at Yasur Volcano (Vanuatu)

J. B. Johnson
Boise State University

T. Boyer
Geolab XP

L. M. Watson
University of Canterbury

J. F. Anderson
Boise State University

AGU ADVANCING EARTH AND SPACE SCIENCE

Geophysical Research Letters®

RESEARCH LETTER
10.1029/2022GL102029

Volcano Opto-Acoustics: Mapping the Infrasound Wavefield at Yasur Volcano (Vanuatu)

J. B. Johnson[1], T. Boyer[2], L. M. Watson[3], and J. F. Anderson[1]

[1]Boise State University, Boise, ID, USA, [2]Geolab XP, Port Vila, Vanuatu, [3]University of Canterbury, Christchurch, New Zealand

Key Points:

- Time series pixel brightness data from cameras show a strong correlation with co-located infrasound records
- Video image processing can be used to extract the spatial infrasound wavefield produced at open-vent volcanoes
- Radiation of sound waves, existence of standing waves, and crater acoustic response may be investigated with volcano opto-acoustics

Supporting Information:

Supporting Information may be found in the online version of this article.

Correspondence to:

J. B. Johnson,
jeffreybjohnson@boisestate.edu

Citation:

Johnson, J. B., Boyer, T., Watson, L. M., & Anderson, J. F. (2023). Volcano opto-acoustics: Mapping the infrasound wavefield at Yasur Volcano (Vanuatu). *Geophysical Research Letters*, *50*, e2022GL102029. https://doi.org/10.1029/2022GL102029

Received 17 NOV 2022
Accepted 23 MAR 2023

Author Contributions:

Conceptualization: J. B. Johnson, T. Boyer, L. M. Watson, J. F. Anderson
Data curation: J. B. Johnson
Formal analysis: J. B. Johnson
Funding acquisition: J. B. Johnson
Investigation: J. B. Johnson, T. Boyer
Methodology: J. B. Johnson, L. M. Watson
Project Administration: J. B. Johnson
Software: J. B. Johnson
Writing – original draft: J. B. Johnson
Writing – review & editing: T. Boyer, L. M. Watson, J. F. Anderson

Abstract We explore the capabilities of volcano opto-acoustics, a promising technique for measuring explosion and infrasound resonance phenomena at open-vent volcanoes. Joint visual and infrasound study at Yasur Volcano (Vanuatu) demonstrate that even consumer-grade cameras are capable of recording infrasound with high fidelity. Passage of infrasonic waves, ranging from as low as 5 Pa to hundreds of Pa, from both explosions and persistent tremor, pressurizes and depressurizes ambient plumes inducing visible vaporization and condensation respectively. Optical tracking of these pressure wavefields can be used to identify spectral characteristics, which vary within Yasur's two deep craters and are distinct for explosion and tremor sources. Wavefield maps can illuminate the propagation of blasts as well as the dynamics of persistent infrasonic tremor associated with standing waves in the craters. We propose that opto-acoustic monitoring is useful for extraction of near-vent infrasound signal and for tracking volcanic unrest from a remote distance.

Plain Language Summary Open-vent volcanoes often have lava lakes or vents where magma is exposed at the bottom of a crater. These volcanoes degas continuously and explode intermittently producing sounds that are low frequency in nature, often below the threshold of human hearing. Such infrasounds are used by volcano scientists to monitor eruptive behavior over time and estimate eruption style and intensity. This current study uses data from Yasur Volcano (Vanuatu) to demonstrate that it is possible to measure infrasound robustly and accurately using cameras, rather than infrasonic microphones. We observe that infrasonic pressure waves induce detectable changes in the clouds or volcanic plume and we process the video imagery to extract infrasound records from remote vantage points. This is an emerging field we call volcano opto-acoustics and it has potential utility for volcano monitoring at other open-vent volcanoes worldwide.

1. Introduction

Yasur is an active, open-vent volcano located on Tanna Island in Vanuatu. Infrasound and audio signals have previously been studied at Yasur by a number of researchers (e.g., Iezzi et al., 2019; Jolly et al., 2017; Kremers et al., 2013; Lorenz et al., 2016; Maher et al., 2022; Marchetti et al., 2013; Meier et al., 2016; Spina et al., 2015), who have primarily focused on the powerful infrasound produced during explosions from multiple vents located at the bottom of the southern crater (Simons et al., 2020) (Figure 1). Yasur's sporadic explosion infrasound, occurring every few minutes, is a persistent feature and is also accompanied by sustained infrasound tremor (e.g., Spina et al., 2015), excited by vents in both craters. Continuous infrasonic tremor may be intense (>1 Pa at 1 km) and is a common feature at many open-vent volcanoes with lava lakes and/or exposed magma columns (e.g., Stromboli (Ripepe et al., 1996), Kilauea (Fee et al., 2010), Villarrica (Rosenblatt et al., 2022), and Etna (Sciotto et al., 2022)). It can be present between explosions and/or when explosions are absent, and may be excited by roiling of the magma surface and/or by vigorous degassing (e.g., Ripepe et al., 2010; Goto & Johnson, 2011). At Yasur, both passive degassing and Strombolian-style explosive degassing are common (e.g., Vergniolle & Metrich, 2022), and their contributions to total gas output has been measured as comparable (i.e., ~60% passive vs. ~40% explosive (Ilanko et al., 2020)).

For volcanoes possessing deep and/or narrow craters degassing may excite resonant infrasound whose spectral composition is modulated by a crater acoustic response controlled by crater shape and sound speed (e.g., Johnson, Watson, et al., 2018; Watson et al., 2019). While it is possible that resonant infrasound originates in natural voids, such as those left after bubble slug bursts (e.g., Kremers et al., 2013; Vergniolle & Brandeis, 1996) or in Helmholtz cavities (e.g., Fee et al., 2010; Goto & Johnson, 2011; Sciotto et al., 2013), resonance is also numerically modeled when crater depth is large compared to diameter (Johnson, Ruiz, et al., 2018; Lyons et al., 2016; Spina

10.1029/2022GL102029

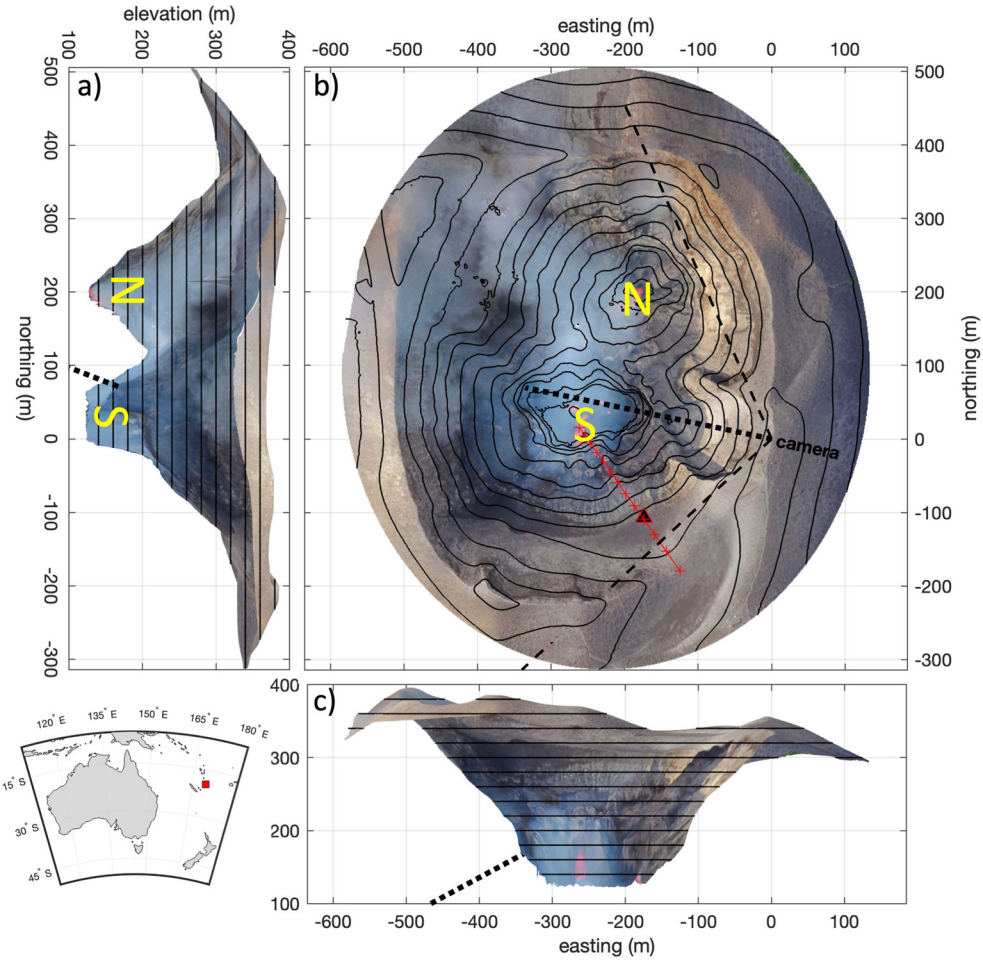

Figure 1. Digital elevation model and draped orthomosaic (1-m resolution) from 10 December 2019. (b) Plan view and (a, c) profile views are shown for north-south and west-east transects respectively. Horizontal field-of-view of the camera and its look direction are indicated with dashed lines. Multiple vents are evident in the south (S) crater and a lava lake is present in the north (N) crater. Map shows Tanna Island's location in the Southwest Pacific.

et al., 2014; Watson et al., 2019). Several studies have reported on crater acoustic response changing with time and attributed this to dynamic crater morphology as magma levels change (e.g., Johnson, Watson, et al., 2018; Richardson et al., 2014; Sciotto et al., 2022; Watson et al., 2020).

Visible blast waves, associated with intense impulsive infrasound, are dramatic manifestations of volcanic explosions and are often observable using conventional, high-speed, or thermal video (e.g., Genco et al., 2014; Marchetti et al., 2013; Taddeucci et al., 2014; Yokoo & Iguchi, 2010). As with chemical explosions, volcano explosion pressure signals begin with compressional pulses (e.g., Johnson & Ripepe, 2011; Matoza et al., 2014), which propagate away from a source and vaporize atmospheric moisture due to adiabatic temperature increase. The compression is typically followed by a rarefaction, where condensation is evident as image brightening. Previous work has studied video brightening (*luminance*) (Yokoo & Ishihara, 2007) and changes in luminance (Yokoo & Taniguchi, 2004) to remotely identify passage of volcanic pressure waves. In a study by Genco et al. (2014) plume luminance of high-speed video was directly related to recorded acoustic signals primarily in the audio band.

In aforementioned studies cloud formation, due to passage of rarefactory pressure waves, appears most evident when plume or clouds are near the dew point and ambient volcanic plume can act as a natural backdrop for optical detection of pressure fluctuations. In this study we showcase the surprising capabilities of consumer-grade video cameras to sample the spatially varying infrasonic pressure wavefield when conditions are appropriate.

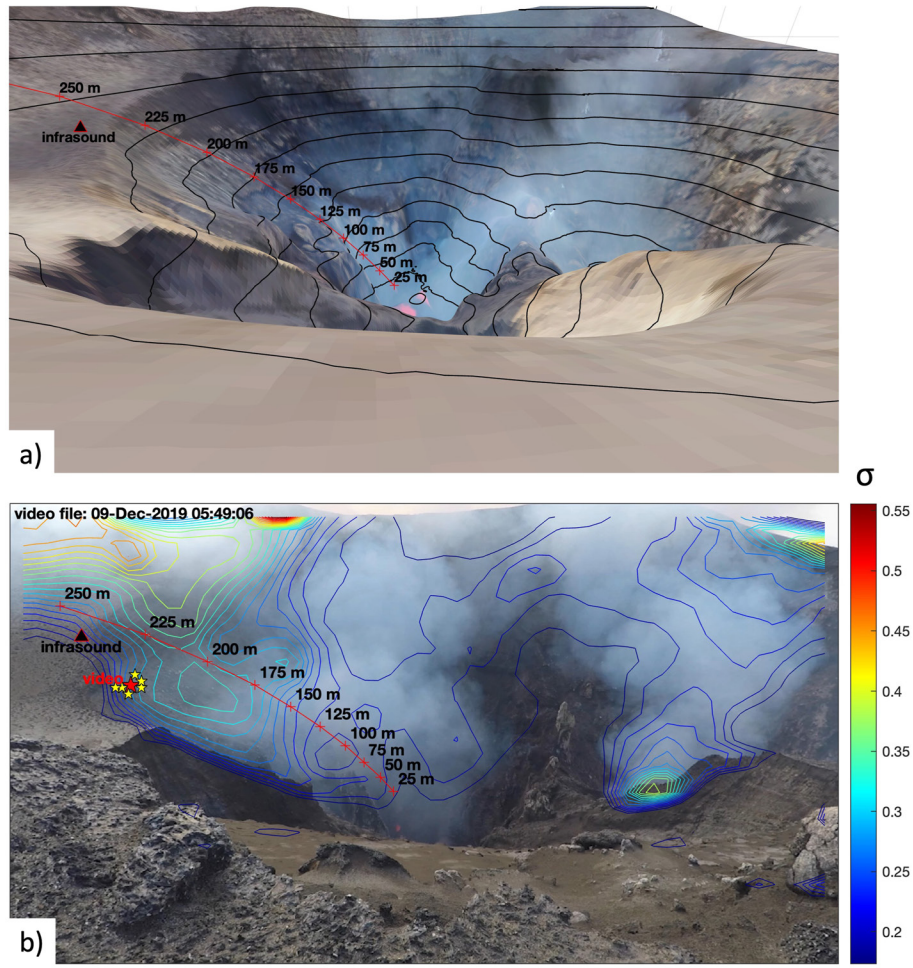

Figure 2. Oblique view digital elevation model along with video image frame. (a) Perspective view is derived from orthophoto-draped topography. (b) Frame from GoPro video shows location of infrasound sensor and video-derived pseudo-infrasound with triangle and stars respectively. Contours indicate standard deviation (σ) of pixel brightness level fluctuations during the video data featured in Figure 3.

2. Data and Signal Processing

Yasur Volcano is an apt natural laboratory for conjoint visual and infrasonic observations. Infrasonic sensors may be placed on the rim and/or just inside the crater (e.g., Maher et al., 2022) whilst camera observations are made from the crater rim from which field-of-view (FOV) may extend nearly to the bottom of the crater(s) (e.g., Turtle et al., 2016; Woitischek et al., 2020). We produced a digital elevation model (DEM) of Yasur's crater area accurate to meter-scale using structure-from-motion (SfM) reconstruction (Figure 1). The DEM was made with 385 images from a quadcopter flying 50–100 m above the crater rim (Figure 1). Perspective views, derived from the DEM, provide scaling and can be oriented to coincide with camera observations (Figure 2).

Infrasound data were collected at a station located within Yasur's crater along with coincident 30 frames per second (fps) video from a GoPro HERO5 Black camera with 1080p resolution set to wide angle FOV. Fish-eye distortion was corrected using a curvature adjustment of −20 within Adobe Premier, which cropped the FOV to 109° (horizontal). The camera was directed at −78° azimuth and downwards at −28° to center on South Crater activity.

While video was recorded for only 2 hr at dusk on 9 December (16:49:06–18:41:47 local time; GMT +11) the infrasound was recorded continuously from 8 to 13 December. Infrasound featured here corresponds to a station located within the camera's FOV and on a terrace ∼160 m above and 150 m SE of the Yasur's south crater (Figure 1). Data are provided for one channel of the three-element array recorded at 400 Hz with a GPS-timed

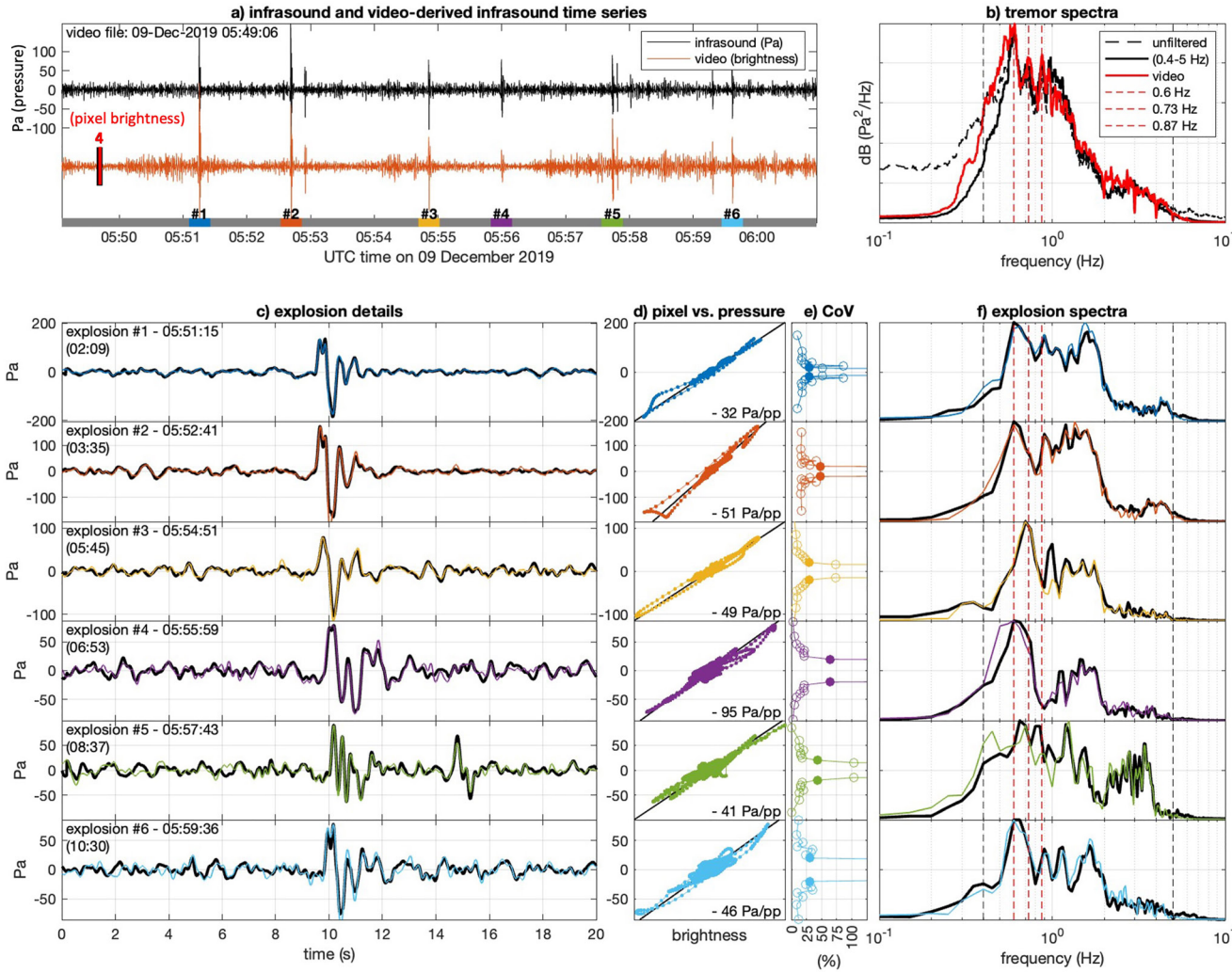

Figure 3. Comparison of infrasound (black lines) and pseudo-infrasound signals (colored lines) corresponding to the location in Figure 2b. (a) Time and (b) frequency domain representations are shown for ∼12 min video. Normalized power spectra are calculated for the waveforms in (a) excepting the six explosion time windows. (c) Detailed 20-s explosion records of infrasound and pseudo-infrasound show waveforms for the biggest transients. (d) Comparison of the infrasound amplitudes and pseudo-infrasound (abscissa) is shown along with regression lines (Pa/pp) relating pressure variation in Pa to brightness color variation (pp). Coefficients of variation are given for different infrasound pressure amplitude bins and suggest that pressure amplitudes exceeding 5–20 Pa are generally correlated with brightness. (f) Normalized power spectra of the six explosion events shows higher frequency components not seen in the tremor spectra of (b).

DiGOS DataCube logger. The infrasonic microphone was an infraBSU version 2 sensor with flat response between 0.1 and 200 Hz Nyquist frequency. Its operation and response are described in Marcillo et al. (2012) and Slad and Merchant (2021). Unfiltered infrasound indicates that the majority (>90%) of energy lies within the 0.4–5 Hz band during our recording period.

We process video by applying a Gaussian smoothing filter (10 pixels) to each 1920 × 1080 image, converting it to grayscale, and then decimating the original 1080p video to 36 × 24 pixels (i.e., 2,304 discrete points). Spatial smoothing averages neighboring pixels within the image to allow sub-integer quantization. We next extract time series from the 2,304 distinct points and filter each pixel's brightness, or intensity/luminance, values in the 0.4–5 Hz band (where recorded infrasound is most prominent). We also apply a cascade of narrow-band notch filters at 1, 2, 3, 4, and 5 Hz, to filter out video artifacts that are common to GoPro and other consumer-grade cameras, which have subtle image brightness artifacts at 1 s intervals (invisible to the eye, but evident in the frequency domain). Amplification of filtered video brightness then allows observation of initially imperceptible oscillations (see supporting information video). Such brightness amplification has been shown to have powerful application for a diverse range of studies in the geoscience and for other applications (Wu et al. (2012)).

The last signal processing step reverses brightness polarity so that image brightening—associated with condensation (and low pressure)—matches the polarity of the rarefactory pressure wave. This is necessary because the explosive compression is associated with darkening of the plume due to temporary heating. Adiabatic pressure/volume relationships of an ideal gas (i.e., PV^{γ} = constant) can be used to derive an estimated temperature change in the atmosphere subjected to a dynamic sound pressure ΔP, that is,

$$\Delta T = T_0 \times \left(\left(\frac{P_0 + \Delta P}{P_0} \right)^{\frac{\gamma-1}{\gamma}} - 1 \right), \quad (1)$$

where T_0 and P_0 are the ambient temperature and pressures, $\gamma = 1.4$ is the heat capacity ratio, and ΔP is the infrasound wave's excess pressure. For an infrasound pressure pulse of $\Delta P = \pm 100$ Pa there may be $\sim \pm 0.08$°C of heating at standard temperatures and pressures and some of this heat is converted to a latent heat of vaporization or condensation for moisture present in the atmosphere (Stull, 2000, p. 44). Our observations and assertions of an infrasonic wave's compressional warming was suggested by Genco et al. (2014) for Stromboli Volcano, but different than Marchetti et al. (2013), who proposed several degrees of cooling associated with Yasur's compressional infrasound. We suggest that their Yasur study, which used thermal video imagery, might not have accounted for the impact of condensation/vaporization on near infrared emissivity.

3. Results

Similarity of infrasound and video-derived infrasound (hereafter referred to as pseudo-infrasound) is remarkable in both time and frequency domains (Figure 3). For the example ~12-min video sequence, which includes both continuous tremor and at least six relatively high-amplitude explosion transients, we compare recorded infrasound to best fit pseudo-infrasound located within the FOV. Best fit is quantified using normalized cross-correlation values between infrasound records (resampled to 100 Hz) and each of the 2,304 pixel-derived time series (also resampled to 100 Hz). Maximum cross-correlation for explosion waveforms and pseudo-infrasound exceeds 0.95 and occurs at locations just a few tens of meters from the infrasound sensor (Figure 2b). The centroid of the six locations from these points is then used as a reference location for pseudo-infrasound records.

A comparison of pseudo-infrasound and infrasound suggests that video brightness may serve as a reliable predictor of pressure; that is, the relationship between pascals and pixel brightness is linear over a wide range of pressures and the scaling factor is constant for short (tens of seconds) time scales during which the background plume is fairly static in terms of color level. The six featured explosions in Figure 3 are used to calculate pressure-to-pixel brightness relationships (Pa/pp), which vary from 32 Pa/pp to 95 Pa/pp. This factor of three variation (during a 12 min time window) indicates that atmospheric conditions, and presence of plume, will affect the capabilities of using opto-acoustics to invert for sound pressure. We acknowledge that in extreme case, such as when plume is absent, pressure waves may become imperceptible.

The threshold for opto-acoustic detection of infrasound waves is of interest and we use a coefficient of variability (CoV) for Pa/pp values to quantify the minimum resolving pressure levels for pseudo-infrasound. CoV is determined as the ratio of standard deviation of Pa/pp to its mean value (i.e., $\mathrm{CoV} = \frac{\sigma_{\mathrm{Pa/pp}}}{\mu_{\mathrm{Pa/pp}}} \times 100\%$) and can be calculated for different pressure level bins. For the explosion data presented in Figure 3e CoVs less than 25%–75% are evident when infrasound pressure is at least 20 Pa. This suggests that 20 Pa is a reliable detection threshold for which opto-acoustics is functional using consumer-grade cameras and similar plume conditions to those presented in this study. At times the persistent tremor, with amplitudes as low as 5 Pa, are also reliably observed in the pseudo-infrasound records (Figures 3d and 3e).

Based upon the good fit between actual infrasound and pseudo-infrasound at the control location (Figure 3), we suggest that cameras may also be used to sample the infrasonic wavefield across a FOV (Figure 4). A single camera's FOV might be used for 2D spatial sampling and to extract spectral content, timing relationships of infrasonic phases, and possible amplitude information. An image map of pixel brightness standard deviation (Figure 2b) gives an indication of those regions where fluctuations in color intensity are substantial enough to reliably sample the passage of infrasound. Notably, high variance corresponds to regions coinciding with a persistent cloud. Because standard deviation in brightness is calculated within the filtered band of interest (e.g., 0.4–5 Hz) it removes contributions and noise from non-infrasonic brightness fluctuations caused by phenomena

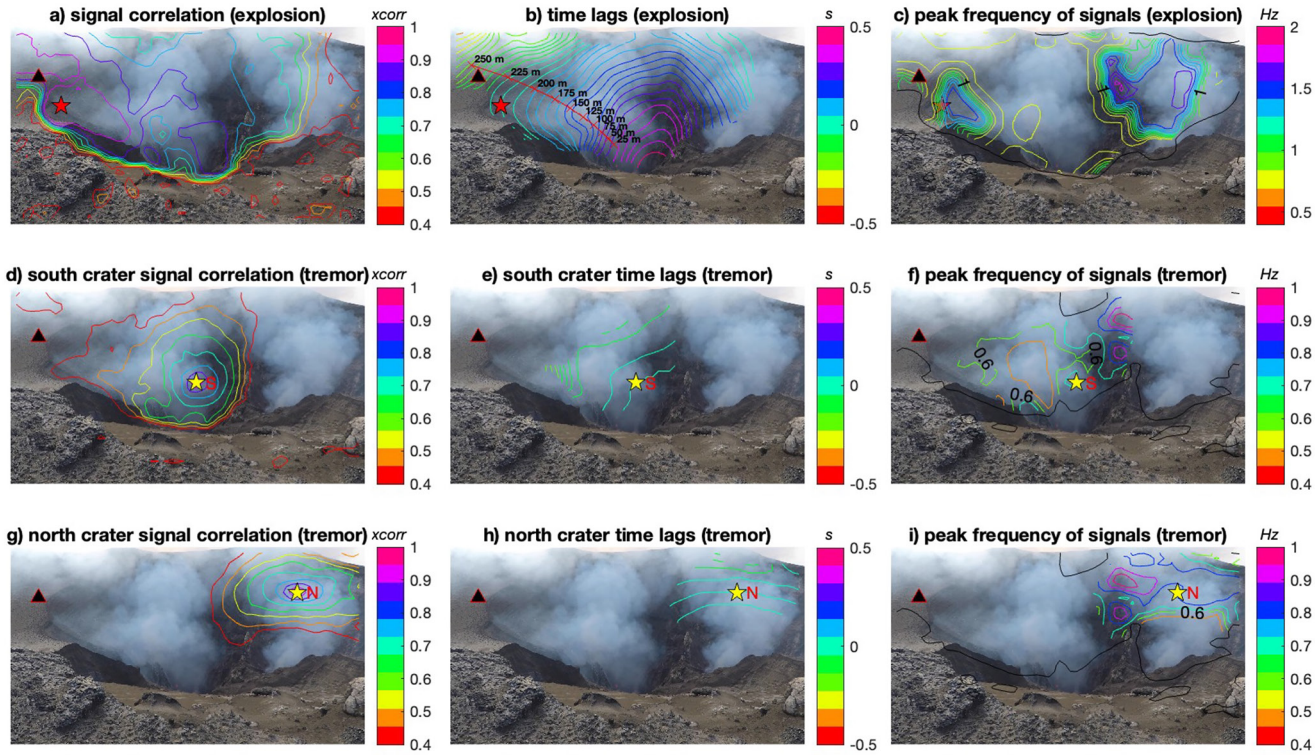

Figure 4. Spatial distribution of infrasound characteristics derived from video. (a) Normalized cross-correlation comparison, relative to star symbol, is shown for all pixels within the field-of-view (for event #1 from Figure 3). (b) Correlated time lags, relative to star, are "mapped" for highly correlated (>0.4) infrasound. (c) Peak frequency of infrasound is provided for highly correlated regions. (d–f) The same data types are displayed as in panels (a–c) except that analyzed signal is ~10 min of tremor and the reference point (star) is moved to the South Crater. (g–i) The same data are displayed as for panels (d–f) except that reference point is in the North Crater.

like plume advection (e.g., Yokoo & Ishihara, 2007), long-term light level shifts, or other transient phenomena (e.g., flying birds and bombs).

We suggest that image maps of cross correlation coefficients, phase lag data, frequency peaks, or other information can be used to understand wave propagation and crater acoustic response during both periods of explosions (Figures 4a–4c) and tremor (Figures 4d–4i). An example explosion from the South Crater of Yasur, for example, exhibits high signal coherence across a broad range of locations, including both craters (Figure 4a). Lag time plots show an expected pattern of approximately hemispherical radiation as sound propagates outward from a South Crater vent (Figure 4b). Spectral peaks are also mappable and indicate values of 0.6–0.8 Hz (within the South crater) and a higher 1.6 Hz mode peripheral to the South Crater.

Analysis of the tremor in Figure 3 is made using reference points in both the South Crater (Figures 4d–4f) and North Crater (Figures 4g–4i). These references are surrounded by relatively small regions of coherence within their respective craters. Nonetheless it is noteworthy that tremor lag delays appear generally small—less than what is observed for radially-spreading explosion infrasound waves (e.g., Figure 4b). This suggests that volcanic tremor pressure disturbances may be largely in phase within each inner crater.

4. Discussion

The relatively small tremor phase delays and their pronounced ~0.55 Hz resonance (Figures 3b, 4f, and 4i) are explainable as resonant standing modes in the two deep craters. Although numerical simulations of the crater acoustic response are beyond the scope of this work, the frequency is consistent with an open-closed pipe whose standing acoustic wavelength λ would be about four times the effective pipe length (e.g., Vidal et al., 2006). Yasur's inner crater is ~160 m deep (Figure 1) giving rise to an inferred infrasound wavelength of ~640 m and a resultant sound speed of 350 m/s for 0.55 Hz sound. Clearly the geometries of Yasur's craters are flared and wider than an idealized narrow pipe, but resonant tones with broadened spectral peaks are still to be expected for

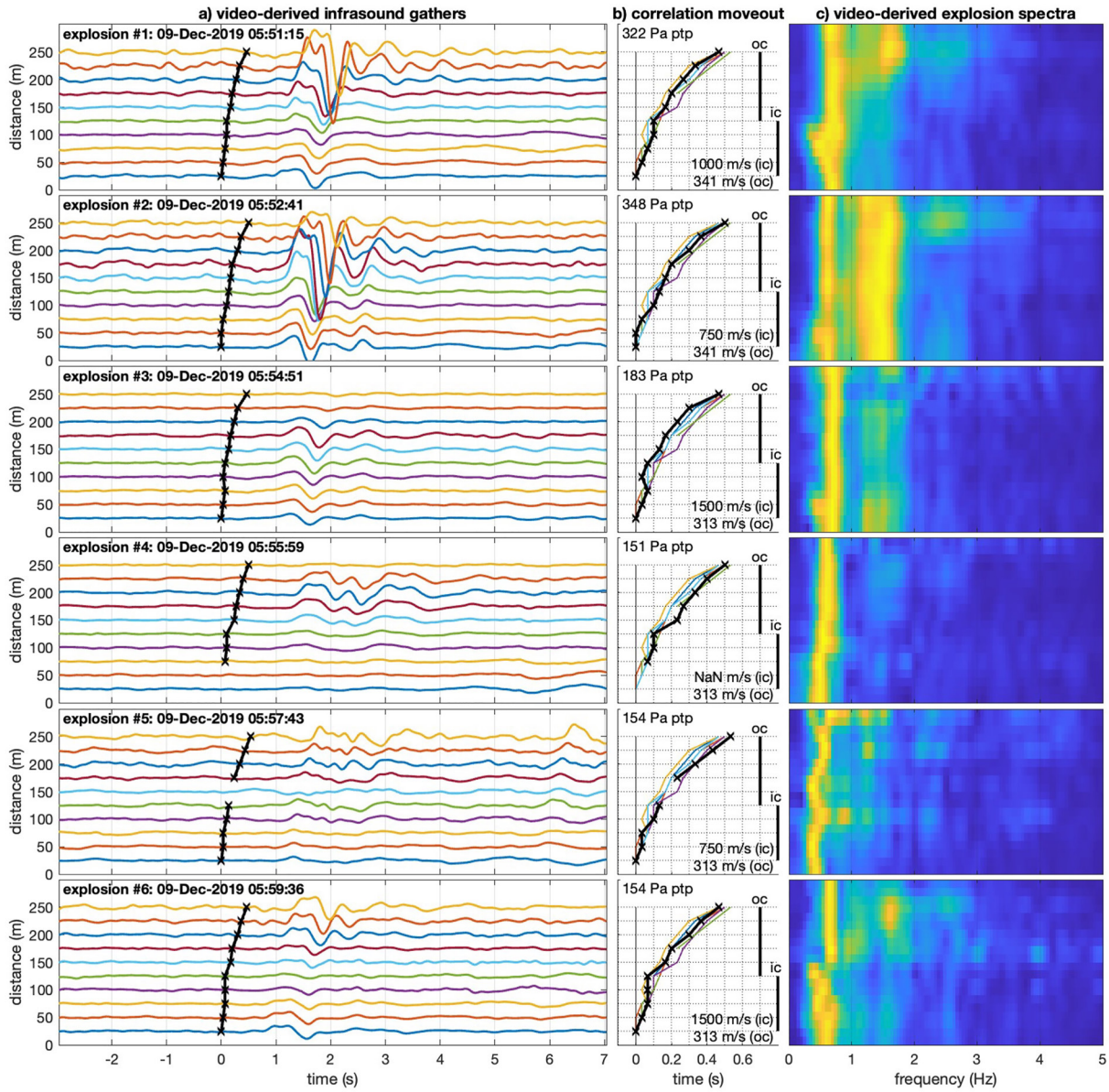

Figure 5. Pseudo infrasound gathers for six explosions sampled along the ten-point profile indicated in Figure 2b. (a) Waveforms are shown using a uniform y-scale across all events. Cross-correlation is used to identify a phase moveout (black line) for the time series. (b) Moveout detail is plotted for pseudo-infrasound; perspective apparent velocities are calculated independently for both inner crater (ic; ≤125 m) and outer crater (oc; ≥125 m). (c) Spectral content, as a function of profile distance, shows both persistent background ~0.55 Hz tremor as well as higher frequency tones associated with explosion transients.

any crater-like geometry with relatively narrow aspect ratios (e.g., Johnson, Ruiz, et al., 2018; Johnson, Watson, et al., 2018).

Joint infrasound and video records intimate that video is capable of spatial sampling of the infrasound wavefield when a plume is present (Figure 5). The capability to optically extract an infrasound gather is exciting because it permits direct measurement of sound propagation in the inner crater without the logistical challenge of direct sampling in a hazardous and inaccessible environment using non-traditional sampling methods liked tethered aerostats (Jolly et al., 2017) or sensors suspended from cables (e.g., Rosenblatt et al., 2022). Although not all volcanoes are ideally suited for optoacoustic sensing many open vent volcanoes—even in arid environments—produce their own plume, which is amenable to camera observations of infrasound. Given an appropriate viewing geometry ambient plume analysis of video-derived infrasound may be useful to extract both sound wave and blast wave phase velocities associated with explosions. A spatially sampled wavefield may then be useful to invert

for explosion sources, which can have significant non-monopole components (e.g., Johnson et al., 2008; Kim et al., 2014, Iezzi et al., 2019).

For the featured six explosions originating in Yasur's South Crater (Figure 3c) we use the distance moveout curves to identify both sonic wave speeds in the vicinity of the outer crater and what initially appears to be supersonic wave speeds internal to the crater (Figure 5b). We define the outer crater (oc) as vent distances between 125 and 250 m, for which video-derived speeds are 313–341 m/s ± 30 m/s and where the error bar is attributable to spatial scaling uncertainties. These speeds and uncertainties in the outer crater are consistent with reasonable sonic velocities and as such we are unable to corroborate the presence of supersonic velocities (372 ± 31 m/s) proposed in Marchetti et al. (2013) for similarly-sized explosions at Yasur.

Although Yasur explosion infrasound may very well possess non-linear propagation attributes (Maher et al., 2022) we do not expect to see significantly supersonic velocities in either the outer crater or inner crater. Peak recorded amplitudes of a few hundred Pa at our infrasound station might reasonably scale back to a few thousand Pa at around 25 m from a vent, but these excess pressures are still too small to give noticeably supersonic propagation. According to the Rankine-Hugoniot relations, Mach number $M = \sqrt{1 + \frac{\gamma+1}{2\gamma}\frac{\Delta P}{P}}$ (Kinney & Graham, 1985) is only ~1.01 for 2,500 Pa pressure. A 1% increase above ambient sonic speeds would be impossible to discern with opto-acoustic techniques.

Our optically-derived speeds within the inner crater (ic) are 750–1,500 m/s (Figure 5b), which are far faster than reasonable supersonic sound speeds and/or for high intrinsic sound speeds (due to the presence of hot crater gases). Crater gas temperature is not expected to exceed a few hundred °C (e.g., Sawyer et al., 2008; Fee et al., 2010) giving rise to sound speeds no faster than ~450 m/s (e.g., Sciotto et al., 2022). The probable explanation for the perceived high velocities ranging from 750 to 1,500 m/s is that they are due to perspective view. Within the inner crater the sound wavefield is not precisely or well sampled along the points shown in the curved arc in Figures 2a and 4b. Rather, a plume with variably thick optical depth is likely responding to infrasound propagating toward the camera. This points to a challenge in sampling a 2D sound wavefield for 3D cloud surfaces.

5. Concluding Thoughts

We demonstrate capabilities of volcano opto-acoustics, a potentially powerful method to spatially sample the infrasound wavefield in a volcanic crater. We suggest that spatial infrasound sampling, which does not require deployment of near-vent infrasonic microphones, opens up possibilities for cameras to be used as a tool to track infrasound propagation, identify infrasound standing waves and tremor, and better understand the crater acoustic response of a volcano. We advocate for further exploration of volcano opto-acoustic's potential. The case study at Yasur serendipitously revealed the potential for accurate infrasound recovery down to ~5–20 Pa using consumer-grade cameras and its potential could be further explored using professional camera imagers (with large CCDs), non-visible wavelength imagers, and/or drone-based video observing sound with plan view perspective. The recent January 2022 paroxysmal Tonga eruption, for instance, showcased the power of remote optical techniques for improved understanding of eruption dynamics (e.g., Carr et al., 2022). While our current study focuses on much smaller-scale volcanic activity both studies argue for the benefits of camera-based quantitative measurements, which could lead to image processing innovation in eruption detection, quantification, and monitoring.

Data Availability Statement

A database with featured waveform data and the original GoPro 710 s video is provided at BSU ScholarWorks with a dedicated DOI (https://doi.org/10.18122/infrasound_data.9.boisestate).

Acknowledgments
Funding for this work was provided by NSF EAR Grant 1830976 while field expenses were covered during filming of National Geographic's *Welcome to Earth episode #1*. Many individuals were critical to data collection, but special recognition goes to J. Lakapas, P. Yamah, W. Smith, and E. Weihenmeyer.

References

Carr, J. L., Horváth, Á., Wu, D. L., & Friberg, M. D. (2022). Stereo plume height and motion retrievals for the record-setting Hunga Tonga-Hunga Ha'apai eruption of 15 January 2022. *Geophysical Research Letters*, *49*(9), 1–7. https://doi.org/10.1029/2022GL098131

Fee, D., Garces, M., Patrick, M., Chouet, B., Dawson, P., & Swanson, D. (2010). Infrasonic harmonic tremor and degassing bursts from Halema'uma'u Crater, Kilauea Volcano, Hawaii. *Journal of Geophysical Research*, *115*(11), B11316. https://doi.org/10.1029/2010JB007642

Genco, R., Ripepe, M., Marchetti, E., Bonadonna, C., & Biass, S. (2014). Acoustic wavefield and Mach wave radiation of flashing arcs in strombolian explosion measured by image luminance. *Geophysical Research Letters*, *41*(20), 7135–7142. https://doi.org/10.1002/2014GL061597

Goto, A., & Johnson, J. B. (2011). Monotonic infrasound and Helmholtz resonance at Volcan Villarrica (Chile). *Geophysical Research Letters*, *38*(6), L06301. https://doi.org/10.1029/2011GL046858

Iezzi, A. M., Fee, D., Kim, K., Jolly, A. D., & Matoza, R. S. (2019). Three-dimensional acoustic multipole waveform inversion at Yasur Volcano, Vanuatu. *Journal of Geophysical Research: Solid Earth*, *124*(8), 8679–8703. https://doi.org/10.1029/2018JB017073

Ilanko, T., Pering, T. D., Wilkes, T. C., Woitischek, J., D'Aleo, R., Aiuppa, A., et al. (2020). Ultraviolet camera measurements of passive and explosive (Strombolian) sulphur dioxide emissions at Yasur Volcano, Vanuatu. *Remote Sensing*, *12*(17), 2703. https://doi.org/10.3390/RS12172703

Johnson, J., Aster, R., Jones, K. R., Kyle, P., & McIntosh, B. (2008). Acoustic source characterization of impulsive Strombolian eruptions from the Mount Erebus lava lake. *Journal of Volcanology and Geothermal Research*, *177*(3), 673–686. https://doi.org/10.1016/j.jvolgeores.2008.06.028

Johnson, J. B., & Ripepe, M. (2011). Volcano infrasound: A review. *Journal of Volcanology and Geothermal Research*, *206*(3–4), 61–69. https://doi.org/10.1016/j.jvolgeores.2011.06.006

Johnson, J. B., Ruiz, M. C., Ortiz, H. D., Watson, L. M., Viracucha, G., Ramon, P., & Almeida, M. (2018a). Infrasound tornillos produced by Volcán Cotopaxi's deep crater. *Geophysical Research Letters*, *45*(11), 1–9. https://doi.org/10.1029/2018GL077766

Johnson, J. B., Watson, L. M., Palma, J. L., Dunham, E. M., & Anderson, J. F. (2018b). Forecasting the eruption of an open-vent volcano using resonant infrasound tones. *Geophysical Research Letters*, *45*(5), 2213–2220. https://doi.org/10.1002/2017GL076506

Jolly, A. D., Matoza, R. S., Fee, D., Kennedy, B. M., Iezzi, A. M., Fitzgerald, R. H., et al. (2017). Capturing the acoustic radiation pattern of strombolian eruptions using infrasound sensors aboard a tethered aerostat, Yasur Volcano, Vanuatu. *Geophysical Research Letters*, *44*(19), 9672–9680. https://doi.org/10.1002/2017GL074971

Kim, K., Lees, J. M., & Ruiz, M. C. (2014). Source mechanism of Vulcanian eruption at Tungurahua Volcano, Ecuador, derived from seismic moment tensor inversions. *Journal of Geophysical Research: Solid Earth*, *119*(2), 1145–1164. https://doi.org/10.1002/2013JB010590

Kinney, G. F., & Graham, K. J. (1985). *Explosive shocks in air*. Springer-Verlag.

Kremers, S., Wassermann, J., Meier, K., Pelties, C., van Driel, M., Vasseur, J., & Hort, M. (2013). Inverting the source mechanism of Strombolian explosions at Mt. Yasur, Vanuatu, using a multi-parameter dataset. *Journal of Volcanology and Geothermal Research*, *262*, 104–122. https://doi.org/10.1016/j.jvolgeores.2013.06.007

Lorenz, R. D., Turtle, E. P., Howell, R., Radebaugh, J., & Lopes, R. M. C. (2016). The roar of Yasur: Handheld audio recorder monitoring of Vanuatu volcanic vent activity. *Journal of Volcanology and Geothermal Research*, *322*, 168–174. https://doi.org/10.1016/j.jvolgeores.2015.06.019

Lyons, J. J., Haney, M. M., Werner, C., Kelly, P., Patrick, M., Kern, C., & Trusdell, F. (2016). Long period seismicity and very long period infrasound driven by shallow magmatic degassing at Mount Pagan, Mariana Islands. *Journal of Geophysical Research: Solid Earth*, *121*(1), 188–209. https://doi.org/10.1002/2015JB012490

Maher, S. P., Matoza, R. S., Jolly, A., de Groot-Hedlin, C., Gee, K. L., Fee, D., & Iezzi, A. M. (2022). Evidence for near-source nonlinear propagation of volcano infrasound from Strombolian explosions at Yasur Volcano, Vanuatu. *Bulletin of Volcanology*, *84*(4), 41. https://doi.org/10.1007/s00445-022-01552-w

Marchetti, E., Ripepe, M., Delle Donne, D., Genco, R., Finizola, A., & Garaebiti, E. (2013). Blast waves from violent explosive activity at Yasur Volcano, Vanuatu. *Geophysical Research Letters*, *40*(22), 5838–5843. https://doi.org/10.1002/2013GL057900

Marcillo, O., Johnson, J. B., & Hart, D. (2012). Implementation, characterization, and evaluation of an inexpensive low-power low-noise infrasound sensor based on a micro-machined differential pressure transducer and a mechanical filter. *Journal of Atmospheric and Oceanic Technology*, *29*(9), 1275–1284. https://doi.org/10.1175/JTECH-D-11-00101.1

Matoza, R. S., Fee, D., & Lopez, T. M. (2014). Acoustic characterization of explosion complexity at Sakurajima, Karymsky, and Tungurahua Volcanoes. *Seismological Research Letters*, *85*(6), 1187–1199. https://doi.org/10.1785/0220140110

Meier, K., Hort, M., Wassermann, J., & Garaebiti, E. (2016). Strombolian surface activity regimes at Yasur volcano, Vanuatu, as observed by Doppler radar, infrared camera and infrasound. *Journal of Volcanology and Geothermal Research*, *322*, 184–195. https://doi.org/10.1016/j.jvolgeores.2015.07.038

Richardson, J. P., Waite, G. P., & Palma, J. L. (2014). Varying seismic-acoustic properties of the fluctuating lava lake at Villarrica volcano, Chile. *Journal of Geophysical Research*, *119*(7), 5560–5573. https://doi.org/10.1002/2014JB011002

Ripepe, M., Marchetti, E., Bonadonna, C., Harris, A. J. L., Pioli, L., & Uliveri, G. (2010). Monochromatic infrasonic tremor driven by persistent degassing and convection at Villarrica Volcano, Chile. *Geophysical Research Letters*, *37*(L15303). https://doi.org/10.1029/2010GL043516

Ripepe, M., Poggi, P., Braun, T., & Gordeev, E. I. (1996). Infrasonic waves and volcanic tremor at Stromboli. *Geophysical Research Letters*, *23*(2), 181–184. https://doi.org/10.1029/95GL03662

Rosenblatt, B. B., Johnson, J. B., Anderson, J. F., Kim, K., & Gauvain, S. J. (2022). Controls on the frequency content of near-source infrasound at open-vent volcanoes: A case study from Volcán Villarrica, Chile. *Bulletin of Volcanology*, *84*(12), 103. https://doi.org/10.1007/s00445-022-01607-y

Sawyer, G. M., Carn, S. A., Tsanev, V. I., Oppenheimer, C., & Burton, M. (2008). Investigation into magma degassing at Nyiragongo volcano, Democratic Republic of the Congo. *Geochemistry, Geophysics, Geosystems*, *9*(2), 1–17. https://doi.org/10.1029/2007GC001829

Sciotto, M., Cannata, A., Gresta, S., Privitera, E., & Spina, L. (2013). Seismic and infrasound signals at Mt. Etna: Modeling the North-East crater conduit and its relation with the 2008-2009 eruption feeding system. *Journal of Volcanology and Geothermal Research*, *254*, 53–68. https://doi.org/10.1016/j.jvolgeores.2012.12.024

Sciotto, M., Watson, L. M., Cannata, A., Cantarero, M., De Beni, E., & Johnson, J. B. (2022). Infrasonic gliding reflects a rising magma column at Mount Etna (Italy). *Scientific Reports*, *12*(1), 16954. https://doi.org/10.1038/s41598-022-20258-9

Simons, B. C., Jolly, A. D., Eccles, J. D., & Cronin, S. J. (2020). Spatiotemporal relationships between two closely-spaced Strombolian-style vents, Yasur, Vanuatu. *Geophysical Research Letters*, *47*(5). https://doi.org/10.1029/2019GL085687

Slad, G., & Merchant, B. (2021). Evaluation of low cost infrasound sensor packages. (Sandia Technical Report SAND2021-13632 701386). https://doi.org/10.2172/1829264

Spina, L., Cannata, A., Privitera, E., Vergniolle, S., Ferlito, C., Gresta, S., et al. (2014). Insights into Mt. Etna's shallow plumbing system from the analysis of infrasound signals, August 2007–December 2009. *Pure and Applied Geophysics*, *172*(2), 473–490. https://doi.org/10.1007/s00024-014-0884-x

Spina, L., Taddeucci, J., Cannata, A., Gresta, S., Lodato, L., Privitera, E., et al. (2015). Explosive volcanic activity at Mt. Yasur: A characterization of the acoustic events (9–12th July 2011). *Journal of Volcanology and Geothermal Research*, *302*, 24–32. https://doi.org/10.1016/j.jvolgeores.2015.06.005

Stull, R. B. (2000). *Meteorology for scientists and engineers* (2nd ed.). Brooks/Cole.

Taddeucci, J., Sesterhenn, J., Scarlato, P., Stampka, K., Del Bello, E., Pena Fernandez, J. J., & Gaudin, D. (2014). High-speed imaging, acoustic features, and aeroacoustic computations of jet noise from Strombolian (and Vulcanian) explosions. *Geophysical Research Letters*, *41*(9), 3096–3102. https://doi.org/10.1002/2014GL059925

Turtle, E. P., Lopes, R. M. C., Lorenz, R. D., Radebaugh, J., & Howell, R. R. (2016). Temporal behavior and temperatures of Yasur volcano, Vanuatu from field remote sensing observations, May 2014. *Journal of Volcanology and Geothermal Research*, *322*, 158–167. https://doi.org/10.1016/j.jvolgeores.2016.02.030

Vergniolle, S., & Brandeis, G. (1996). Strombolian explosions 1. A large bubble breaking at the surface of a lava column as a source of sound. *Journal of Geophysical Research*, *101*(B9), 20433–20447. https://doi.org/10.1029/96jb01178

Vergniolle, S., & Metrich, N. (2022). An interpretative view of open-vent volcanoes. *Bulletin of Volcanology*, *84*(9), 83. https://doi.org/10.1007/s00445-022-01581-5

Vidal, V., Géminard, J. C., Divoux, T., & Melo, F. (2006). Acoustic signal associated with the bursting of a soap film which initially closes an overpressurized cavity: Experiment and theory. *The European Physical Journal B*, *54*(3), 321–339. https://doi.org/10.1140/epjb/e2006-00450-0

Watson, L. M., Dunham, E. M., & Johnson, J. B. (2019). Simulation and inversion of harmonic infrasound from open-vent volcanoes using an efficient quasi-1D crater model. *Journal of Volcanology and Geothermal Research*, *380*, 64–79. https://doi.org/10.1016/j.jvolgeores.2019.05.007

Watson, L. M., Johnson, J. B., Sciotto, M., & Cannata, A. (2020). Changes in crater geometry revealed by inversion of harmonic infrasound observations: 24 December 2018 eruption of mount Etna, Italy. *Geophysical Research Letters*, *47*(19). https://doi.org/10.1029/2020GL088077

Woitischek, J., Woods, A. W., Edmonds, M., Oppenheimer, C., Aiuppa, A., Pering, T. D., et al. (2020). Strombolian eruptions and dynamics of magma degassing at Yasur Volcano (Vanuatu). *Journal of Volcanology and Geothermal Research*, *398*, 106869. https://doi.org/10.1016/j.jvolgeores.2020.106869

Wu, H. Y., Rubinstein, M., Shih, E., Guttag, J., Durand, F., & Freeman, W. (2012). Eulerian video magnification for revealing subtle changes in the world. *ACM Transactions on Graphics*, *31*(4), 1–8. https://doi.org/10.1145/2185520.2185561

Yokoo, A., & Iguchi, M. (2010). Using infrasound waves from eruption video to explain ground deformation preceding the eruption of Suwanosejima volcano, Japan. *Journal of Volcanology and Geothermal Research*, *196*(3–4), 287–294. https://doi.org/10.1016/j.jvolgeores.2010.08.008

Yokoo, A., & Ishihara, K. (2007). Analysis of pressure waves observed in Sakurajima eruption movies. *Earth Planets and Space*, *59*(3), 177–181. https://doi.org/10.1186/BF03352691

Yokoo, A., & Taniguchi, H. (2004). Application of video image processing to detect volcanic pressure waves: A case study on archived images of Aso volcano, Japan. *Geophysical Research Letters*, *31*(23), 4. https://doi.org/10.1029/2004GL021183